Geomechanics and Engineering, *Vol. 34, No. 6 (2023) 683-696*
https://doi.org/10.12989/gae.2023.34.6.683

Simulation of the fracture of heterogeneous rock masses based on the enriched numerical manifold method

Yuan Wang[1], Xinyu Liu*[2], Lingfeng Zhou[2] and Qi Dong[1]

[1]*College of Water Conservancy and Hydropower Engineering, Hohai University, Nanjing, Jiangsu 210024, China*
[2]*College of Civil and Transportation Engineering, Hohai University, Nanjing, Jiangsu 210024, China*

(*Received June 29, 2023, Revised August 9, 2023, Accepted August 16, 2023*)

Abstract. The destruction and fracture of rock masses are crucial components in engineering and there is an increasing demand for the study of the influence of rock mass heterogeneity on the safety of engineering projects. The numerical manifold method (NMM) has a unified solution format for continuous and discontinuous problems. In most NMM studies, material homogeneity has been assumed and despite this simplification, fracture mechanics remain complex and simulations are inefficient because of the complicated topology updating operations that are needed after crack propagation. These operations become computationally expensive especially in the cases of heterogeneous materials. In this study, a heterogeneous model algorithm based on stochastic theory was developed and introduced into the NMM. A new fracture algorithm was developed to simulate the rupture zone. The algorithm was validated for the examples of the four-point shear beam and semi-circular bend. Results show that the algorithm can efficiently simulate the rupture zone of heterogeneous rock masses. Heterogeneity has a powerful effect on the macroscopic failure characteristics and uniaxial compressive strength of rock masses. The peak strength of homogeneous material (with heterogeneity or standard deviation of 0) is 2.4 times that of heterogeneous material (with heterogeneity of 11.0). Moreover, the local distribution of parameter values can affect the configuration of rupture zones in rock masses. The local distribution also influences the peak value on the stress–strain curve and the residual strength. The post-peak stress–strain curve envelope from 60 random calculations can be used as an estimate of the strength of engineering rock masses.

Keywords: heterogeneous; numerical manifold method; rock masses; rupture zone

1. Introduction

Geological materials such as rock masses are highly heterogeneous and widely used in geotechnical engineering. They contain multi-scale defects (Zhou *et al.* 2014), such as inclusions (Cook 1965), internal pores (Tsang and Witherspoon 1981), and microscopic or macroscopic fractures (Wang *et al.* 2020). These defects add variability to the engineering properties of the material, such as strength and other physical and mechanical properties (Shemirani *et al.* 2017, Baud *et al.* 2014, Xue *et al.* 2020), which may significantly affect soil-structure interaction (Shi *et al.* 2019, Shi *et al.* 2022, Shi *et al.* 2023). Engineering problems, especially those that involve small quantities of materials such as rock masses, do not usually account for heterogeneity explicitly. The problem is usually simplified; homogeneity is assumed and average values of material properties are used. When the representative volume is much larger than the volume involved in the problem, the assumption of homogeneity is inadequate, and a precise representation of the heterogeneity of the properties becomes vitally important.

Over the past decades, researchers have improved the efficiency of simulations of fractures and deformation in heterogeneous rock masses (Tang 1997, Chen *et al.* 2004, Zhu and Tang 2006, Ma and An 2008, Xiong *et al.* 2011, Jiao *et al.* 2015, Yu *et al.* 2020). These studies have important geotechnical engineering applications. The use of the Finite Element Method (FEM) to study material heterogeneity began in the late 1960s. Internal structure of materials has been characterized using various joint element and interface element models, including Goodman's joint elements (Goodman *et al.* 1968), six-node fracture elements (Li *et al.* 2017), and interface elements in contact mechanics (Katona 1983). Azarafza *et al.* (2021) proposed a machine vision and image processing-based approach for determining grain size and distribution, which has been used to identify granular sediment gradation distribution. Artificial intelligence (AI) image processing (Azarafza *et al.* 2019) has also been used to categorize the discontinuities of rock blocks into two groups (opened and closed), and has considerably reduced errors. Wu *et al.* (2019) adopted a Voronoi tessellation technique in the numerical manifold method (NMM), generating random polygonal grains to better approximate rock microstructure. Wu *et al.* (2020) developed a numerical manifold model to simulate the dynamics of saturated and semi-saturated porous media, which are commonly encountered in engineering problems. Liu *et al.* (2021) used a discrete fracture network model in NMM to simulate grout penetration in fractured rock masses. These studies examined rock mechanical properties by modeling rock internal structure on a small scale. However, simulations on

*Corresponding author, Research Student
E-mail: hou196inm@163.com

ISSN: 2005-307X (Print), 2092-6219 (Online)

Table 1 Comparison of methods used to simulate macroscopic failure of rock masses

Method	Advantages	Disadvantages
XFEM (Patil *et al*. 2019)	No need to remeshing	Unable to handle multiple crack propagation and coupling
Peridynamics (Ouchi *et al*. 2015)	High accuracy and efficiency in solving macro/micro discontinuous mechanical problems analysis	Difficult to directly simulate structure from a macro perspective
Smoothed Particle Hydrodynamics (SPH) (Ma *et al*. 2011)	No fixed grid,	Need to set a pressure constant in the state equation manually
RFPA (Tang 2011)	Able to simulate progressive material failure, Consider heterogeneity	The crack growth is a quasistatic process, ignoring the influence of inertia force caused by rapid growth
NMM (Ma *et al*. 2010)	Simultaneous handling of continuous and discontinuous problems	The value of contact spring stiffness is sensitive to the rate of convergence of the solution

larger scales may require considerable amounts of computational resources.

Numerous scholars have used numerical models to characterize heterogeneous materials by incorporating physical and mechanical parameters that are heterogeneous to describe the internal structure of the materials. Mesoscale heterogeneity can be accurately represented by the heterogeneity index of statistical models. For example, Yang *et al.* (2022) used ABAQUS to simulate the impact of heterogeneity on the characteristics of ubiquitiformal cracks during the Brazilian rock splitting test. The Weibull distribution has also been widely used to characterize material heterogeneity, for example, in the popular rock mechanics software Rock Failure Process Analysis (RFPA) (Tang *et al.* 1998, Tang *et al.* 2000, Tang *et al.* 2000). Tang *et al.* (2000) developed RFPA, which is based on FEM. The introduction of heterogeneous properties allows RFPA to simulate the nonlinear deformation of quasi-brittle behavior with an ideal brittle constitutive law for rock masses. To examine the physical mechanisms underlying the discrepancies in rock tension, Liao *et al.* (2019) carried out three-dimensional RFPA simulations of the direct tension test, Brazilian test, and three-point bending test of intact heterogeneous rock. To study the heterogeneity of concrete failure, a spatial correlation length factor was added to the conventional Weibull distribution (Tang *et al.* 2009). By combining linear elastic material constitutive relations with statistical heterogeneous models at the mesoscale, Tang *et al.* (1998) accurately predicted the nonlinear deformation and failure behaviors of rock at the macroscale.

Unprecedented developments in numerical simulation technology provide a strong foundation for the study of the macroscopic failure of rock masses in the present day. Numerical methods can solve complex problems that cannot be solved by analytical methods. Various continuum-based numerical methods have been developed over the decades; they include FEM, the finite difference method (FDM), the boundary element method (BEM), and other meshless methods. Among these methods, FEM is the most widely used in engineering because it can be used to set up complex constitutive models with complex boundary conditions to solve dynamic problems. However, FEM also has drawbacks. The finite element mesh must align with fractures. Mesh generation requires considerable amounts of work and remeshing is unavoidable in simulations of fracture growth. Considering all these shortcomings, FEM is not the ideal tool for the simulation of fracture evolution. To overcome these drawbacks, especially in meshing, much effort has been put into modifying the conventional FEM. One famous example is the extended finite element method (XFEM) (Zi and Belytschko 2003). The XFEM is based on the partition of unity (PU). It introduces discontinuous enrichment functions into the conventional FEM approximation to avoid remeshing during discontinuity development. Another example is the generalized finite element method (GFEM) (Strouboulis *et al.* 2000, Strouboulis *et al.* 2001).

The NMM is based on the mathematical concept of manifold and the finite cover approximation theory. It uses truncated discontinuous shape functions to solve continuous medium problems, fractured medium problems, and block system problems in a unified format, building a bridge that connects continuity and discontinuity (Ma *et al.* 2010). The NMM uses two covers—a physical and a mathematical—that are separate for less restrictive meshing. Most of the current research on the NMM focuses on crack propagation in homogeneous materials (Chiou *et al.* 2002, Ma *et al.* 2009, Zhang *et al.* 2010). Wang *et al.* (2003) simulated crack extension using a first-order cover function and accurately calculated the length of crack extension at each computational step. Wu *et al.* (2017) used the NMM to characterize the mechanical response of rock mass under uniaxial compression. Zhang *et al.* (2002) used the NMM to investigate crack generation and expansion in dams with homogeneous mechanical properties. Table 1 summarizes the advantages and disadvantages of the numerical methods that have been used to simulate the macroscopic failure of rock masses.

Some efforts have also been made to extend the NMM to study the influence of heterogeneous conditions on rock failure (Yang *et al.* 2016, Yang *et al*. 2018, Yang *et al*. 2020, Wu *et al.* 2019, Wu *et al*. 2020). These studies are focused on the spread of internal cracks in rocks. The decrease in computational efficiency with crack expansion hinders the application of NMM to large-scale engineering projects.

In this study, we present the enriched NMM, which uses the heterogeneity index of a statistical model to take into account heterogeneous material properties. It can be used to

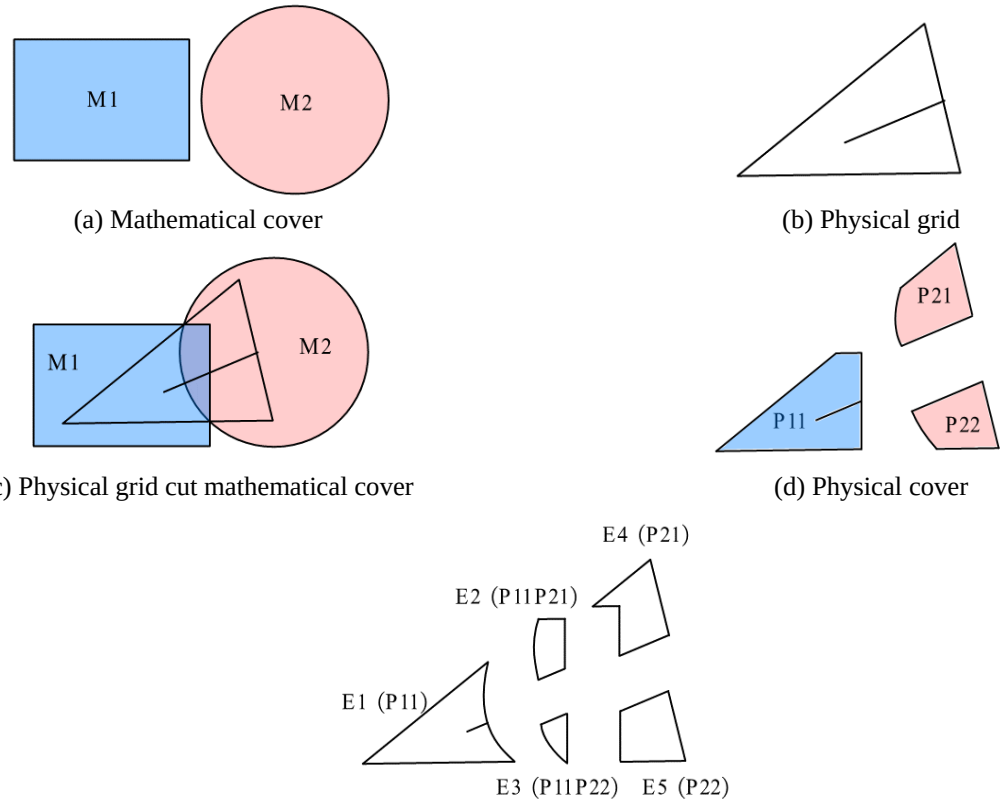

(a) Mathematical cover

(b) Physical grid

(c) Physical grid cut mathematical cover

(d) Physical cover

(e) Manifold elements

Fig. 1 Formation of manifold elements

study the fracture processes of rock masses and the mechanical responses to the processes. Existing NMM crack extension simulations require constant updating of the fracture elements and their cover information for both sides of the crack and are computationally expensive. We present a novel algorithm to simulate the rupture zone in rock masses. The new algorithm efficiently characterizes the macroscopic failure of rock masses as a cumulative process of the failure of multiple elements. It is an efficient and cost-effective method for simulating macroscopic failure.

2. Basic NMM theory

Detailed explanation of the theory of NMM can be found in Shi (1991). In this section, we present a simple example to illustrate the basic concepts of NMM and the generation of manifold elements. In this example, the mathematical covers are a rectangle (M1) and a circle (M2) (Fig. 1(a)). The physical grid (i.e., the actual computational domain) is a triangle with one crack (Fig. 1(b)). The NMM covering system has the advantage of not needing to divide the computational grid to match the grid to the computational domain. The NMM system only requires the complete coverage of the physical grid by the mathematical covers; areas of overlap between the physical grid and the mathematical covers form the physical cover and manifold elements (Figs. 1(c)-1(e)). Discontinuities in the physical grid can be easily characterized using NMM because the mathematical cover can be split by the boundaries as well as the internal cracks of the physical grid. The crack in the physical grid splits the mathematical cover M2 into two independent physical covers (P21 and P22) and partially cuts into the mathematical cover M1 to form the physical cover P11 (Fig. 1(d)). As a result, five manifold elements, namely E1 (P11), E2 (P11P21), E3 (P11P22), E4 (P21), and E5 (P22), are formed (Fig. 1(e)).

3. Enriched numerical manifold method for Heterogeneous rock masses

3.1 Heterogeneous algorithm based on random theory

The NMM assumes that materials are linear elastic and homogeneous bodies and uses the incremental method to calculate model strain. We used the NMM to develop a model for heterogeneous materials by incorporating a heterogeneous algorithm based on random theory.

The heterogeneous algorithm for different physical and mechanical parameters—elastic modulus, internal friction angle, and cohesion—of heterogeneous rock masses was generated following two steps. First, we used random theory to generate arrays of parameter values that conform to a specific distribution. Second, the data arrays were discretized and incorporated into the model.

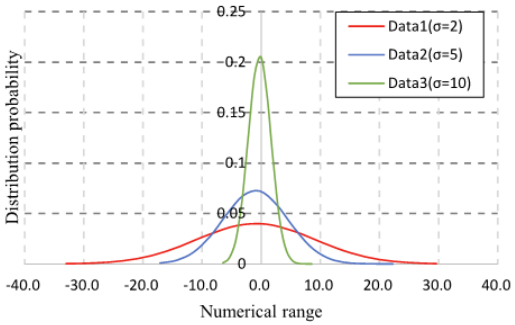

Fig. 2 Schematic diagram of the probability distribution of number sets following the normal distribution

The physical and mechanical properties of the manifold elements in the numerical manifold model were assumed to follow the normal distribution

$$\chi(\alpha)=[exp\left(-(\alpha-\alpha_0)^2/2\sigma^2\right)]/\sqrt{2\pi}\,\sigma \tag{1}$$

where α is the physical or mechanical property of the manifold element; α_0 is the position parameter, which is the mean value of the property; σ is the scale parameter, which is the standard deviation of the property.

The programming language C was used to extend the NMM program. To facilitate programming, we used the Box–Muller algorithm to implement a probability function that follows the normal distribution; Z is a set of random numbers in the interval (0, 1) that follows the standard normal distribution; it was mapped to the statistic φ with mean μ and standard deviation σ as follows

$$\varphi=\mu+\left(Z\cdot\sigma\right) \tag{2}$$

Fig. 2 shows the distribution of the number sets under the influence of three different σ values (2, 5, and 10).

The random number discretization method is commonly used to discretize spatial coordinates according to the Gaussian integral points. In the NMM, the traditional Gaussian integral is replaced by simplex integral, which is more efficient. Therefore, Gaussian coordinates are unsuitable for data discretization in the NMM. Because the NMM uses regular mathematical meshes (e.g., triangular meshes), we discretized data using the following manifold element center co-ordinate discretization method

$$despersed\left[\varphi_i\right]\rightarrow E_i center:\left(x_i,y_i\right) \tag{3}$$

where $E_i center$ is the center of the i^{th} manifold element.

3.2 Rupture zone algorithm

Rock fracture behavior is usually modeled using the elastic–brittle constitutive law and the modified Mohr–Coulomb criterion. The Mohr–Coulomb criterion is widely used in rock mechanics to determine rock damage under compression. However, it can only consider the shear failure of rock masses under compression and ignores the influence of intermediate principal stress. As illustrated by the shaded area I in Fig. 3(a), shear failure occurs under

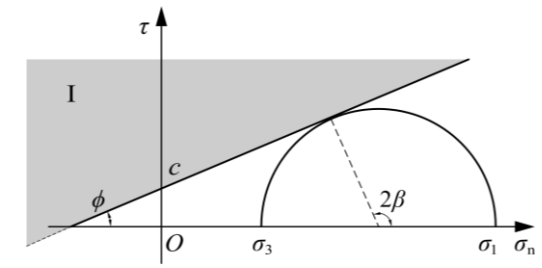

(a) Mohr–Coulomb criterion

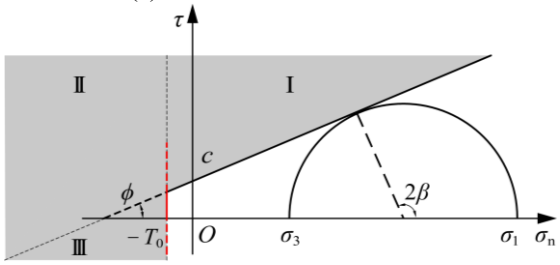

(b) Modified Mohr–Coulomb criterion

Fig. 3 Failure criterion of Manifold Element

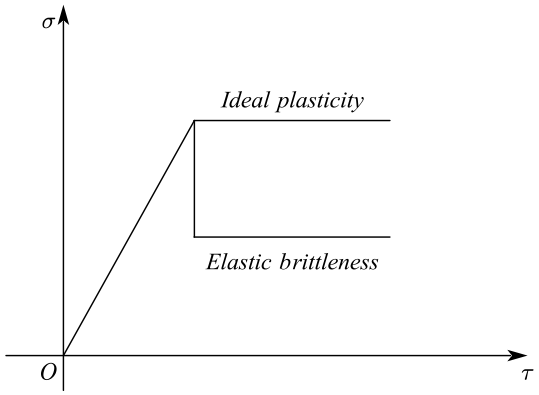

Fig. 4 Elastic–brittle constitutive curve

stress states that lie beyond the fracture line. Thus, the Mohr–Coulomb criterion cannot be used to determine tensile damage of rock masses. To enable the simulation of shear and tensile damage, we modified the Mohr–Coulomb criterion to include a tensile cutoff. The modified criterion is shown in Figure 3 (b). The shaded area represents failure and can be divided into three blocks; block I represents complete shear failure; block II represents the coexistence of shear and tensile failure, and block III represents complete tensile failure. The modified Mohr–Coulomb criterion takes into account rock tensile strength T_0 and tensile failure occurs when the minor principal stress exceeds the tensile strength

$$\begin{cases}\sigma_3\le -T_0\\ \left((\sigma_1-\sigma_2)/2\right)\ge c\cdot\cos\phi+\left((\sigma_1+\sigma_3)/2\right)\cdot\sin\phi, -T_0<\sigma_3\end{cases} \tag{4}$$

In real-life engineering situations, external loads can damage the internal structure of rock masses and lead to reductions in compressive strength and elastic modulus, fracture, expansion of primary cracks, and other changes.

We developed a damage algorithm for the elastic

Table 2 Physical and mechanical properties of the heterogeneous rock masses in the Four-Point Shear Beam (FPSB) and the Semi-Circular Bend (SCB)

Example name		Elastic modulus, E (GPa)	Cohesion, c (MPa)	Internal friction angle, ϕ (°)	Poisson Ratio, μ	Tensile strength, T_0 (MPa)
FPSB	Mean value	27.9	5.5	63	0.19	-
	Standard deviation, σ	2.0	1.22	2.24	-	-
SCB	Mean value	42	5.5	63	0.19	30
	Standard deviation, σ	2.0	1.22	2.24	-	2.0

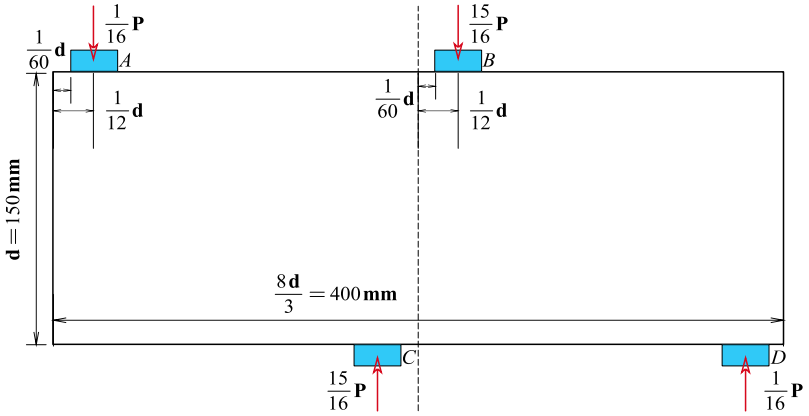

Fig. 5 Schematic diagram of the Four-Point Shear Beam (FPSB)

modulus of the manifold element to describe the corresponding changes in the internal characteristics of heterogeneous rock masses. The damage algorithm is based on the elastic–brittle constitutive law (Fig. 4).

In the numerical manifold model, stresses in the manifold elements are calculated using the following incremental method

$$\begin{cases} \Delta\sigma_x = \dfrac{E}{1-\mu^2}\left(\Delta\varepsilon_x + \mu\Delta\varepsilon_y\right) \\ \Delta\sigma_y = \dfrac{E}{1-\mu^2}\left(\mu\Delta\varepsilon_x + \Delta\varepsilon_y\right) \\ \Delta\tau_{xy} = \dfrac{E}{2(1+\mu)}\Delta\gamma_{xy} \end{cases} \tag{5}$$

The use of the incremental method results in stress accumulation in the manifold elements. Elements that meet the failure criterion may have a reduced elastic modulus, but the final stress value may not reflect characteristics of brittle damage. As a result, we modified the algorithm and introduced a damage variable D to reduce the elastic modulus when the failure criterion is met

$$E' = E(1-D) \tag{6}$$

The damage variable is the stiffness degradation parameter of the failing element. Introduction of the damage variable allows the algorithm to simulate nonlinear stress–strain behavior during rock failure by resetting stress and reducing the elastic modulus. Under uniaxial tensile stress, D of the manifold element is expressed as (Zhu and Tang 2004)

$$D = \begin{cases} 0, \varepsilon < \varepsilon_{c0} \\ 1 - \dfrac{\varepsilon_{c0}\lambda}{\varepsilon}, \varepsilon \geq \varepsilon_{c0} \end{cases} \tag{7}$$

where ε_{c0} is the strain when compressive stress reaches the uniaxial compressive strength f_{c0} and λ is the residual strength coefficient.

After failure, the stiffness and stress of the damaged manifold elements are set to zero. If the stress state of the damaged element shows recompression, the corresponding stiffness is restored to a certain degree, allowing the element to transmit stress under loading. Substituting Eq. (6) into Eq. (5) gives

$$\begin{cases} \Delta\sigma_x = \dfrac{E(1-D)}{1-\mu^2}\left(\Delta\varepsilon_x + \mu\Delta\varepsilon_y\right) \\ \Delta\sigma_y = \dfrac{E(1-D)}{1-\mu^2}\left(\mu\Delta\varepsilon_x + \Delta\varepsilon_y\right) \\ \Delta\tau_{xy} = \dfrac{E(1-D)}{2(1+\mu)}\Delta\gamma_{xy} \end{cases} \tag{8}$$

3.3 Validation of the proposed algorithm

We applied the algorithm to the examples of the Four-Point Shear Beam (FPSB) and the Semi-Circular Bend (SCB) to validate its ability to simulate the rupture of heterogeneous rock masses. The material parameters of the two examples are summarized in Table 2.

Most natural rock masses are in compression and shear

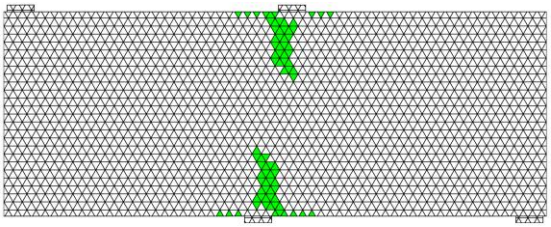

(a) Rupture zone calculated with the enriched NMM (time=2.1 s)

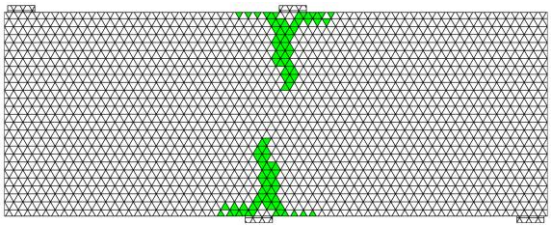

(b) Rupture zone calculated with the enriched NMM (time=2.3 s and 6.9 s)

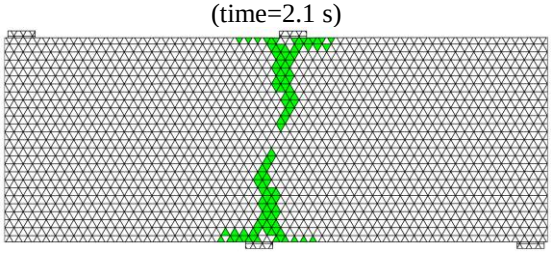

(c) Rupture zone calculated with the enriched NMM (time=7.2 s)

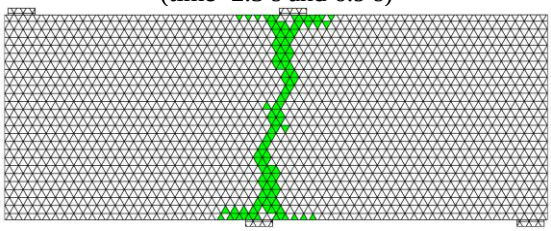

(d) Rupture zone calculated with the enriched NMM (time=7.4 s)

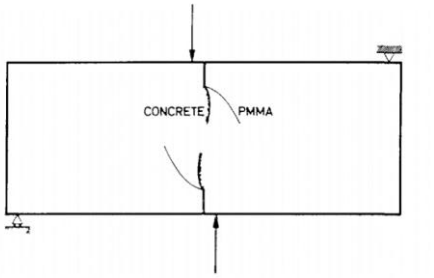

(e) Experimental results from the literature

Fig. 6 Rupture zones (green) of the Four-Point Shear Beam (FPSB)

failure is the most common form of rock damage. In addition to the conventional uniaxial compression test, the FPSB is also often used to study shear damage of specimens, especially in concrete structures. Bocca *et al.* (1990), Schlangen *et al.* (1992), and others have conducted numerical simulation studies of the damage process of the FPSB.

We used a two-dimensional NMM program to set up the FPSB model (Fig. 5) during pre-processing. The ratio of the two loads on the upper part of the FPSB was set to 1:15 (Melin 1989). The NMM pre-processing meshing function created an FPSB model with 3,200 manifold elements.

Manifold elements that meet the Mohr–Coulomb criterion are considered as damaged and are marked in green, forming the rupture zone in Fig. 6. Simulation results show that the FPSB is in central symmetric shear failure. The rupture zone is located halfway along the width of the beam, near loading blocks B and C. Failure takes place in three stages. The first stage is from 0 to 2.3 s. During this stage, the beam is under shear loading. Failure first occurs near the loading blocks B and C and the fractures are perpendicular to the top and bottom surfaces of the beam. As the load increases, stress accumulates inside the two-dimensional NMM model; the fracture in the top part of the beam grows in parallel to the one in the bottom part. Figs. 6(a) and 6(b) shows the rupture zone at 2.1 and 2.3 s, respectively. The second stage is from 2.3 to 6.9 s. During this stage, the beam is under shear loading, but no new manifold element meets the failure criterion, and the rupture zone stops growing. The third stage is from 6.9 to 7.4 s. During this stage, the beam is damaged further. At 6.9 s, the fractures in the top and bottom parts of the beam gradually grow toward each other. Fig. 6(c) shows the rupture zone at 7.2 s. Finally, stresses are equivalent to the shear strength of the beam and a continuous fracture runs between the top and bottom surfaces of the beam at 7.4 s, connecting the two initial fractures (Fig. 6(d)).

Melin *et al.* (1989) reported the results of a laboratory FPSB experiment. The final failure mode and fracture development in the experiment are consistent with the rupture zones and their development in the enriched NMM (Fig. 6(e)). This confirms that our algorithm can reproduce the shear failure of the loaded FPSB.

The SCB is an effective means to test the tensile strength of brittle materials, such as rocks (Ayatollahi et al. 2006). We used the NMM program to set up a two-dimensional numerical manifest model of the SCB with homogeneous physical and mechanical properties (Fig. 7).

We made a number of simplifications to improve the modeling of the half-disc tensile test. These simplifications include: (1) using fixed triangular supports instead of bearing tables; (2) using loading plates instead of concentrated loads to prevent stress concentration inside the manifold element. The loading rate was set to 0.02 mm/s (Huang *et al*. 2021, Lim *et al*. 1993).

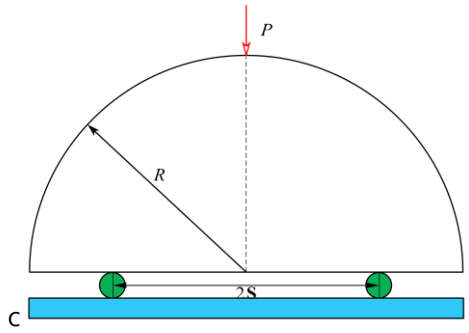

Fig. 7 Schematic diagram of the Semi-Circular Bend (SCB)

Simulation results are shown in Fig. 8(a). Tensile fracture in the SCB starts at the bottom of the disc. As loading increases, the rupture zone grows toward the loading point at the top of the disc, and a continuous rupture zone finally connects the top and bottom parts of the semi-circular disc (Figs. 8(b)-8(d)). Fig. 8(e) shows the SCB at final failure in laboratory experiments as reported in the literature (Ayatollahi *et al.* 2006). There is a close agreement between Figs. 8(d) and 8(e). Thus, we infer that our algorithm can be used to model tensile rupture zone and shear damage with reasonable accuracy.

4. Description of numerical parametric study

4.1 Parameter values

After algorithm validation, we used the algorithm to set up a uniaxial compression model without surrounding pressure. We conducted a series of parametric tests to investigate the nonlinear characteristics of the damage process of rock masses and the evolution of manifold element damage.

Table 3 summarizes the values that were used in the parametric study; A-0 is the control group. It is made of homogeneous materials and is used to compare with the results of groups B and C, which are made of heterogeneous materials. To explore the influence of heterogeneity on peak/post-peak strength, stress–strain curve, and rupture zone configuration of rock masses, we kept the heterogeneity (σ) and distribution of cohesion and internal friction angle invariant, and varied the heterogeneity of the elastic modulus. We compared the results from A-0, B, and C to explore the influence of heterogeneity on rock properties, especially on the elastic modulus. In addition, we conducted three random calculations (A-1, A-2, and A-3) using the same heterogeneity to explore the impact of different random distributions of heterogeneous parameters on peak/post-peak strength, stress–strain curves, and rupture zone configuration. We also conducted multiple random calculations (total of 60) using the same heterogeneity ($\sigma = 2.0$); they are not shown in Table 3. Different discrete results can be obtained for each calculation by using a random algorithm to generate a heterogeneous array of strength parameter values. Thus, we kept the distribution of

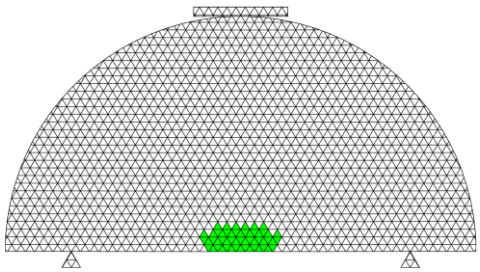

(a) Rupture zone calculated with the enriched NMM (time=2.5 s)

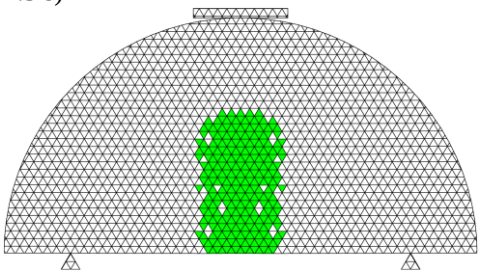

(b) Rupture zone calculated with the enriched NMM (time=3 s)

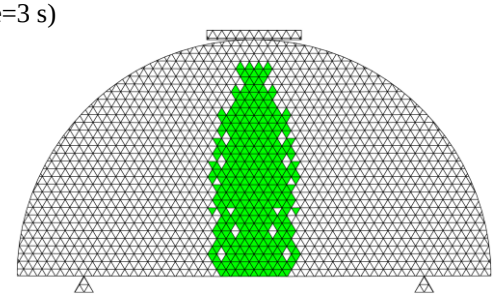

(c) Rupture zone calculated with the enriched NMM (time=3.5 s)

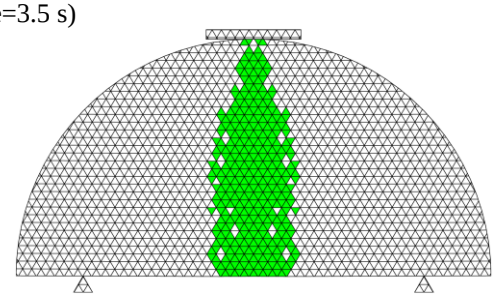

(d) Rupture zone calculated with the enriched NMM (time=4.6 s)

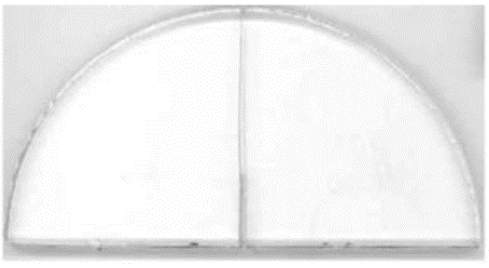

(e) Experimental results from the literature

Fig. 8 Rupture zones (green) of the Semi-Circular Bend (SCB)

cohesion and internal friction angle invariant and varied the distribution of elastic modulus.

To explore the influence of the local discrete state in the heterogeneous model on rock failure, a random algorithm

Table 3 Values used in numerical parametric study of uniaxial compression model

Group name		Elastic modulus, E (GPa)	Cohesion, c (MPa)	Internal friction angle, ϕ (°)	Poisson Ratio, μ
A-0	Mean value	42	5.5	63.0	0.19
	Standard deviation, σ	-	1.22	2.24	-
A-1 (A)	Mean value	42	5.5	63.0	0.19
	Standard deviation, σ	2	1.22	2.24	-
A-2	Mean value	42	5.5	63.0	0.19
	Standard deviation, σ	2	1.22	2.24	-
A-3	Mean value	42	5.5	63.0	0.19
	Standard deviation, σ	2	1.22	2.24	-
B	Mean value	42	5.5	63.0	0.19
	Standard deviation, σ	5	1.22	2.24	-
C	Mean value	42	5.5	63.0	0.19
	Standard deviation, σ	11	1.22	2.24	-

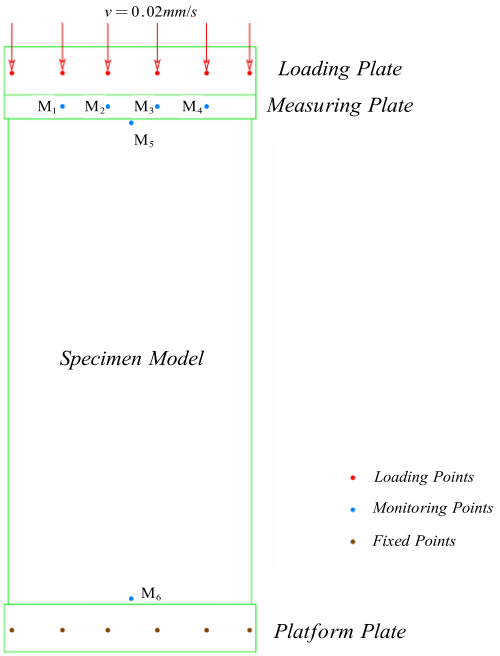

Fig. 9 Schematic diagram of uniaxial compression model

was used to generate three random calculations—A-1, A-2, and A-3—using the same heterogeneity. To study the influence of heterogeneity on the failure characteristics and compressive strength of rock masses, two groups of B and C tests were set up and their results were compared with those from A-1.

4.2 Numerical model of uniaxial compression

The uniaxial compression model is shown in Fig. 9. Displacement loading was applied at a controlled rate. At each time step, loading was applied at a uniform rate. Stress was measured at M1, M2, M3, and M4, and displacement was measured at M5 and M6.

Following Huang *et al.* (2021) and the results from many similar tests that we have conducted, the loading rate was set at 0.02 mm/s.

5. Results of numerical parametric study

5.1 Effects of discrete distributions of parameter values on macroscopic failure characteristics

Elastic modulus was one of the heterogeneous parameters that was examined in the parametric study. Fig. 10 shows the discrete distributions of elastic modulus values in the comparative models A-1, A-2, and A-3. Although the models were parameterized using the same standard deviation for the elastic modulus at the macroscale (Table 3), they had different local distributions of elastic modulus values, which will give considerably different results at different steps of the calculation. Therefore, we used the random algorithm to generate different random sample models even for the heterogeneous models that used the same means and standard deviations.

Three separate numerical calculations (A-1, A-2, and A-3) were performed using the values in Table 3 and the damage process is shown in Fig. 11. Over time, the damaged manifold elements (in green) connect with each other to form a continuous rupture zone. Different local distributions of elastic modulus values result in different configurations of the rupture zone, and the differences can be substantial. The penetrating fracture zone often appears along the 45° plane. The location of this oblique rupture zone depends on the distribution of parameter values inside the sample. There is a tendency for failure to start in the weakest part of the sample. Because of the randomness of the mechanical properties of microscopic elements, Fig. 11 shows completely different final failure modes for three heterogeneous samples with the same macroscopic physical and mechanical properties. The local distribution of mechanical parameter values affects the mode of macroscopic failure and also affects the time and speed of macroscopic failure to a certain extent.

Fig. 12 shows the stress–strain curves of A-1, A-2, and A-3. The effect of local elastic modulus values on macroscopic mechanical response is more prominent around and after peak stress. Rock mass peak and residual strengths depend on the discrete distributions of parameter

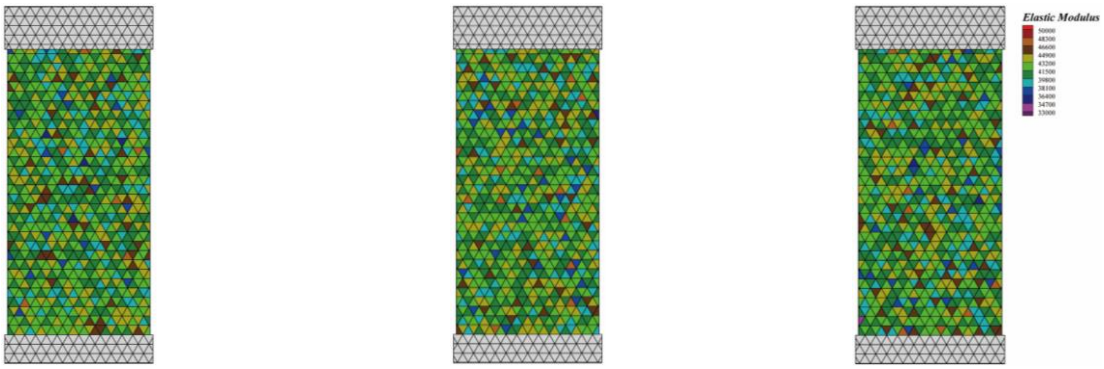

(a) A-1 (b) A-2 (c) A-3

Fig. 10 Three models of heterogeneous rock masses with different discrete distributions of elastic modulus values

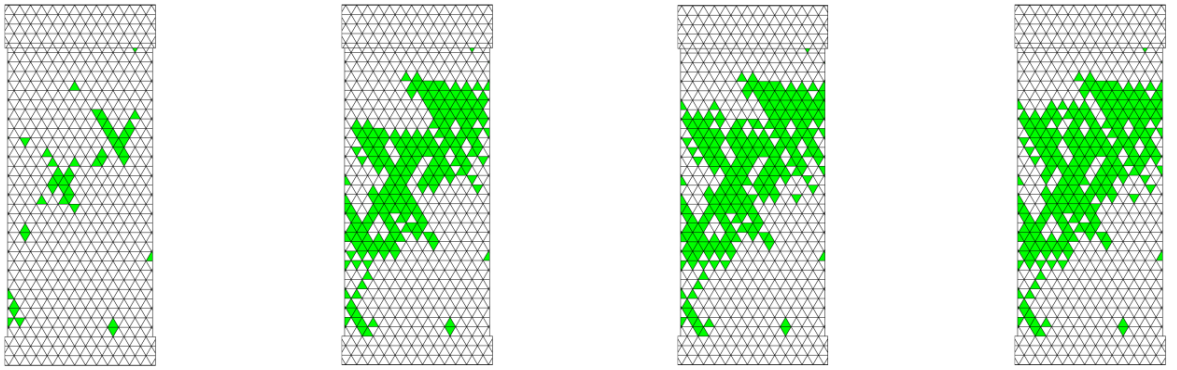

(i) time = 2.3 s (ii) time = 2.5 s (iii) time = 2.7 s (iv) time = 3.6 s

(a) Rupture zone of A-1

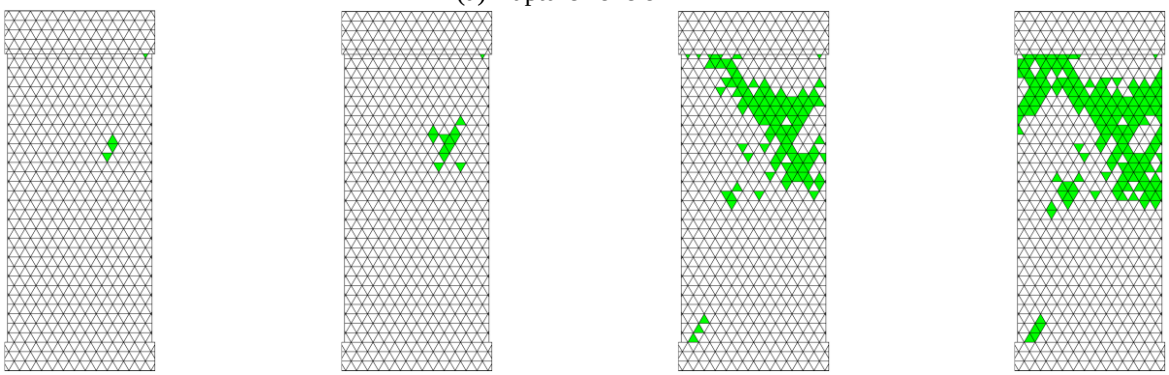

(i) time = 2.0 s (ii) time = 2.3 s (iii) time = 2.5 s (iv) time = 2.6 s

(b) Rupture zone of A-2

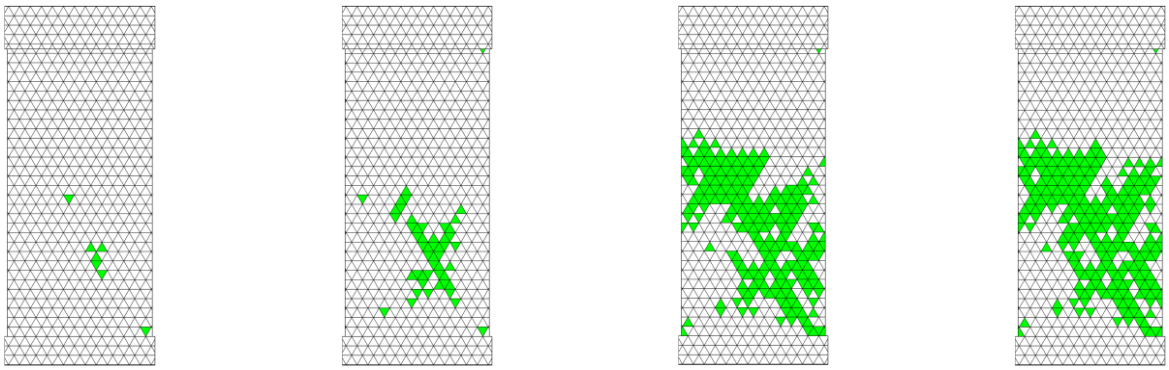

(i) time = 2.3 s (ii) time = 2.5 s (iii) time = 2.7 s (iv) time = 2.9 s

(c) Rupture zone of A-3

Fig. 11 Effects of discrete distributions of parameter values on macroscopic failure characteristics

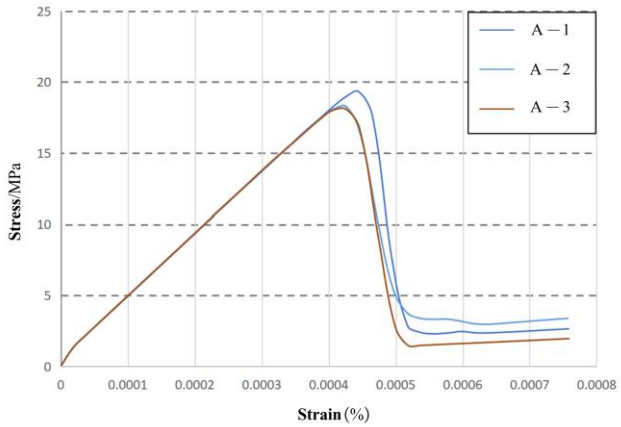

Fig. 12 Stress–strain curves of A-1, A-2, and A-3

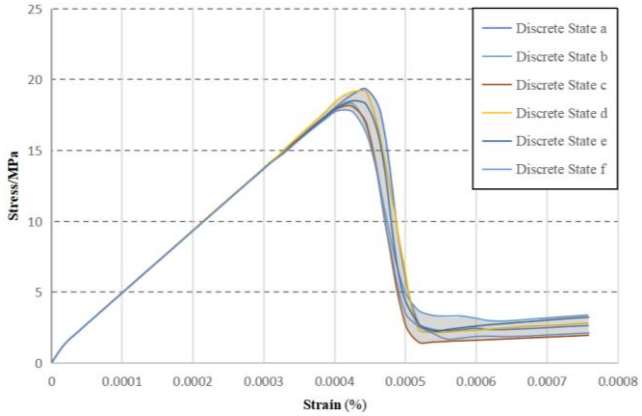

Fig. 13 Envelope of stress-strain curve for the rock masses with the same heterogeneity

values inside the sample, which vary between samples. The macroscopic compressive strengths of A-1, A-2, and A-3 are within 7% of one another, although the different distributions of parameter values inside samples have led to different macroscopic failure characteristics.

5.2 Stress–strain curve envelope

We conducted 60 random calculations using the same heterogeneity. While the local distributions of elastic modulus values vary, the stress–strain curves are all within the same envelope (gray shading in Fig. 13). This indicates that the numerical model can reproduce a reasonable strength envelope that is consistent with reality using the same heterogeneity. Our enriched NMM can be used to estimate rock mass strength values and envelopes for engineering projects on the basis of on-site measurements of the physical and mechanical parameters of the rock masses. Estimates of strength values and envelopes can be used to improve the reliability, safety, and financial viability of engineering projects during the design phase

5.3 Effects of heterogeneity on macroscopic failure characteristics

Fig. 14 shows the local distributions of elastic modulus values for A-0, A, B, and C (Table 3). The control group A-

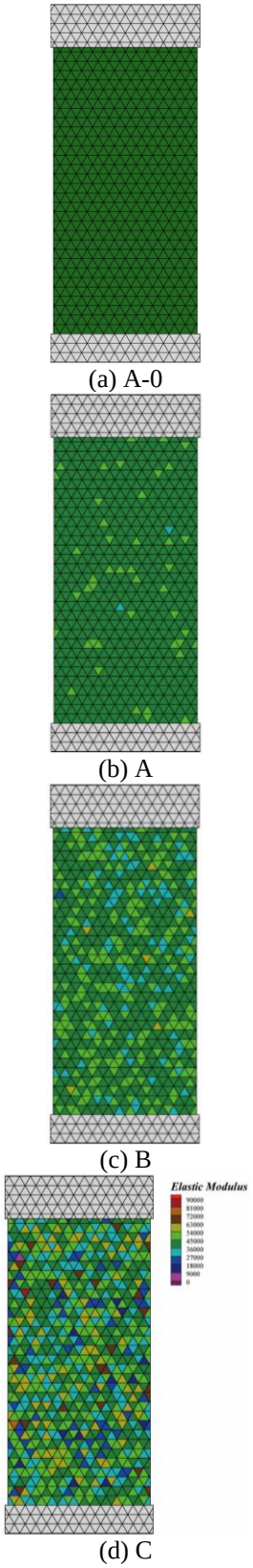

Fig. 14 Distributions of elastic modulus values in A-0, A, B, and C

0 has a symmetrical X-type rupture zone, which is typical of homogeneous materials. To study the effects of heterogeneity on the macroscopic failure and strength of

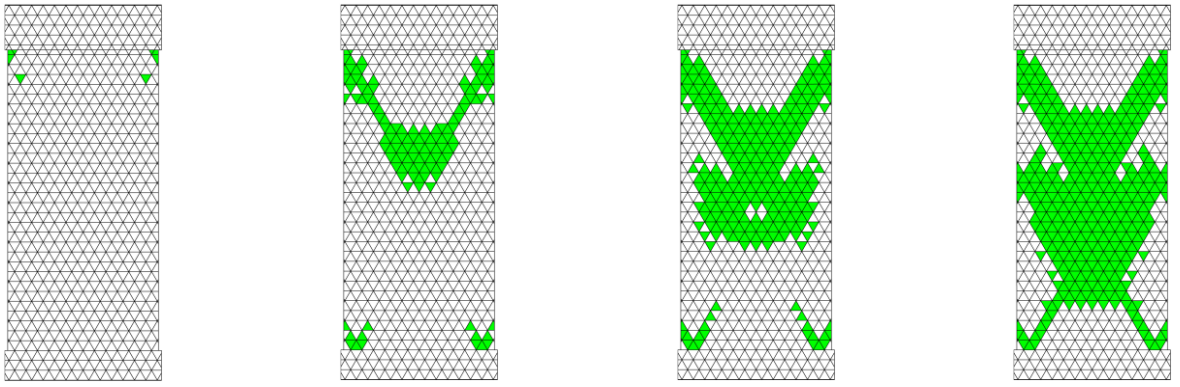

(i) time = 3.8 s (ii) time = 4.0 s (iii) time = 4.2 s (iv) time = 4.9 s

(a) Rupture zone of A-0

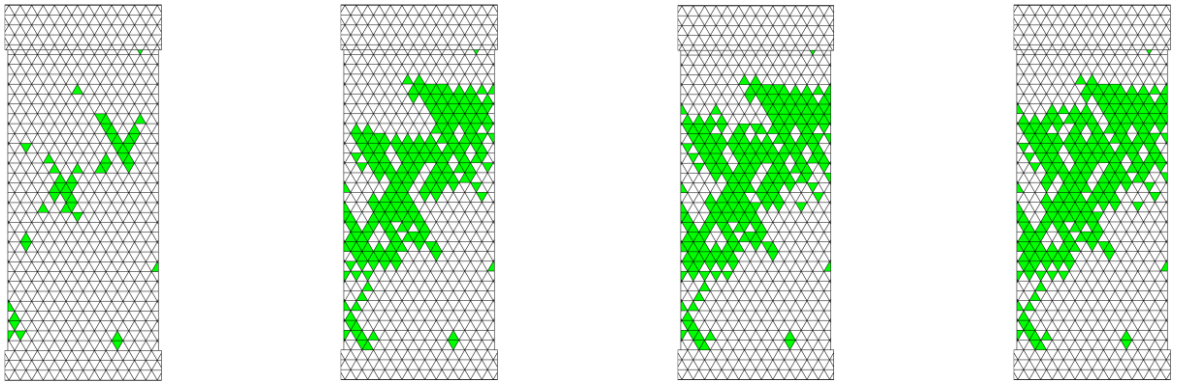

(i) time = 2.3 s (ii) time = 2.5 s (iii) time = 2.7 s (iv) time = 3.6 s

(b) Rupture zone of A

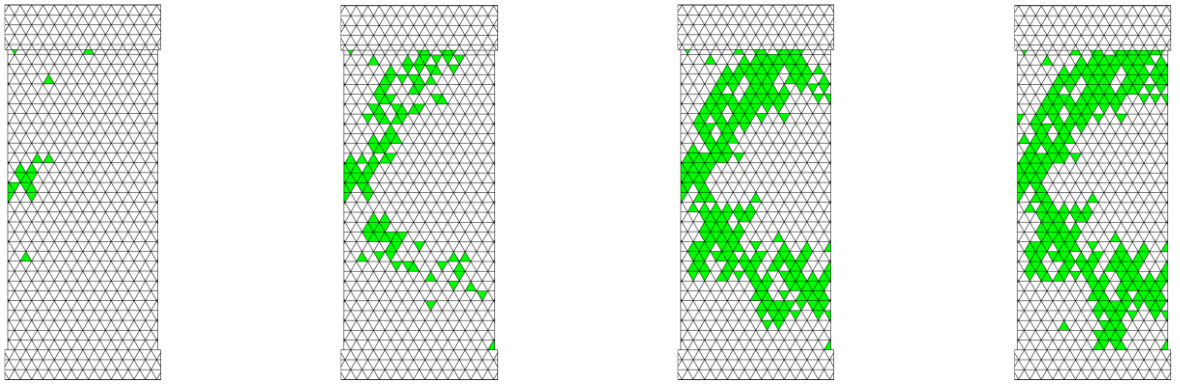

(i) time = 2.1 s (ii) time = 2.3 s (iii) time = 2.5 s (iv) time = 3.0 s

(c) Rupture zone of B

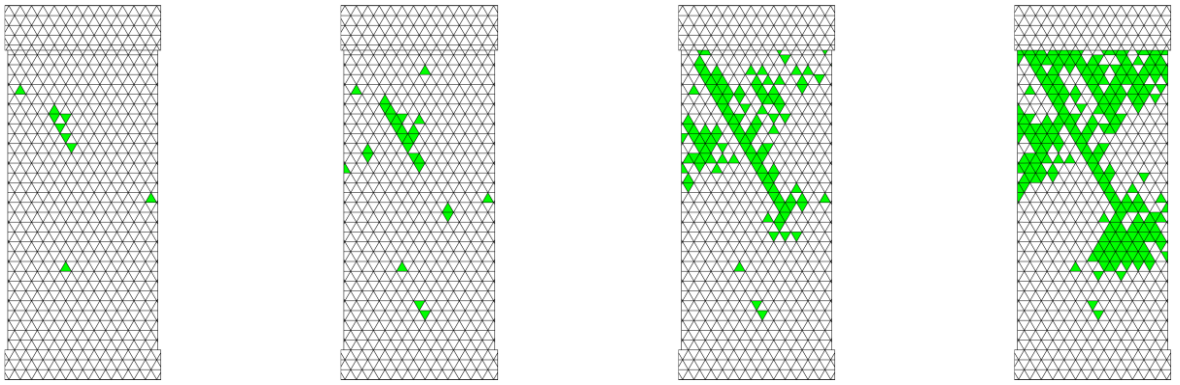

(i) time = 1.5 s (ii) time = 1.7 s (iii) time = 1.9 s (iv) time = 2.3 s

(d) Rupture zone of C

Fig. 15 Effects of heterogeneity on macroscopic failure characteristics

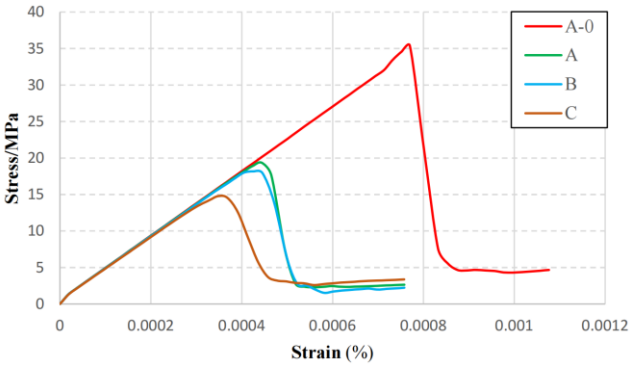

Fig. 16 Stress–strain curves of A-0, A, B, and C

rock masses, we compared the results of A-0 with those from A-1 (A), B, and C.

Comparison of the results of A-0, A, B, and C shows that a higher standard deviation is associated with a higher level of discretization of the internal parameter distribution. Fig. 15 shows the development of rupture zones in the simulations of the heterogeneous materials—A, B, and C. The green triangles indicate damaged manifold elements. The rupture zones of the heterogeneous materials do not have the X-type symmetry that is present in the rupture zone of the homogeneous material. With increased heterogeneity, macroscopic failure occurs earlier and at a higher speed.

The heterogeneous materials (A, B, and C) have the same macroscopic properties as the homogeneous material (A-0). However, strength in A-0 is considerably higher than the strength in A, B, or C, highlighting the importance of the consideration of material heterogeneity in the design of engineering projects. Moreover, high standard deviation is associated with high inhomogeneity in heterogeneous rock masses and enhanced nonlinearity in the stress–strain curve.

The stress–strain curve of A-0 clearly shows the characteristics of brittle failure; post-peak stress decreases rapidly and stabilizes at the level of residual strength. At a standard deviation of 11.0, there is a considerable decrease in peak stress; higher inhomogeneity is associated with earlier failure and decreased brittle damage.

The peak strengths of A-0, A, B, and C are 35.4, 19.3, 18.2, and 14.8 MPa, respectively. The peak strength of the homogeneous material A-0 ($\boldsymbol{\sigma = 2.0}$) is 2.4 times that of the heterogeneous material C ($\boldsymbol{\sigma = 11.0}$). Moreover, the post-peak strength of A-0 is almost twice that of C. Thus, heterogeneity affects the peak strength of rock materials and the residual strength of heterogeneous material is lower than that of homogeneous material. However, the stress–strain curves of A, B, and C show that residual strength varies little with heterogeneity in heterogeneous materials.

6. Conclusions

In this study, we presented an enhanced numerical manifest model that can effectively simulate the rupture zone in heterogeneous rock masses. This provides a cost-effective and efficient method to simulate rock failures on large scales. A rupture zone simulation algorithm was introduced into the NMM by using a modified Mohr–Coulomb criterion with tensile cutoff and the intrinsic relationship of manifold element damage. We draw the following conclusions, which are based on our simulation results:

- We used the FPSB and SCB tests to evaluate the performance of our enriched numerical manifold model in reproducing shear and tensile damage. There was a close agreement between our model results and experimental results published in the literature.
- Our enriched numerical manifold model improves on the NMM by considering heterogeneity in the physical and mechanical characteristics of materials. It can accurately simulate rock fractures and is suitable for the simulation of rock masses with heterogeneous properties.
- The local distribution of elastic modulus values influences the post-peak damage characteristics and stress–strain curves and gives rise to a vast variety of rupture zone configurations. Post-peak stress–strain curve and peak and residual strengths vary with local distributions of elastic modulus values.
- We conducted 60 NMM simulations using the same heterogeneity. Simulated stress–strain curves all fall within the same envelope, which is consistent with the engineering properties of natural rock masses. The simulated strength values and envelope correspond to the possible values of similar types of rock materials, indicating that our enriched numerical manifold model can be used in the geological monitoring of engineering projects.
- As the heterogeneity of rock mass increases, the nonlinearity of the stress–strain curve also increases, causing a gradual reduction in the peak value on the stress–strain curve. Moreover, the peak strength of homogeneous rock material is higher than that of heterogeneous material. Thus, the characterization of heterogeneous materials is essential for practical engineering applications. In addition to reducing the strength of heterogeneous rock masses, heterogeneity also affects the time and speed of rock mass failure. High heterogeneity is associated with early failure and high failure rate.

Acknowledgments

This research was supported by the National Natural Science Foundation of China (U2240210).

References

Ayatollahi, M.R., Aliha, M.R.M. and Hassani, M.M. (2006), "Mixed mode brittle fracture in PMMA—an experimental study using SCB specimens", *Mater. Sci. Eng. : A*, **417**(1-2), 348-356. https://doi.org/10.1016/j.msea.2005.11.002.

Azarafza, M., Ghazifard, A., Akgün, H. and Asghari-Kaljahi, E. (2019), "Development of a 2D and 3D computational algorithm for discontinuity structural geometry identification by artificial intelligence based on image processing techniques", *Bull. Eng.*

Geol. Environ., **78**(5), 3371-3383. https://doi.org/10.1007/s10064-018-1298-2.

Azarafza, M., Nanehkaran, Y.A., Akgün, H. and Mao, Y. (2021), "Application of an image processing-based algorithm for river-side granular sediment gradation distribution analysis", *Adv. Mater. Res.*, **10**(3), 229-244. https://doi.org/10.12989/amr.2021.10.3.229.

Baud, P., Wong, T.F. and Zhu, W. (2014), "Effects of porosity and crack density on the compressive strength of rocks", *Int. J. Rock Mech. Min. Sci.*, **67**, 202-211. https://doi.org/10.1016/j.ijrmms.2013.08.031.

Bocca, P., Carpinteri, A. and Valente, S. (1990), "Size effects in the mixed mode crack propagation: softening and snap-back analysis", *Eng. Fract. Mech.*, **35**(1-3), 159-170. https://doi.org/10.1016/0013-7944(90)90193-K.

Chen, S., Yue, Z.Q. and Tham, L.G. (2004), "Digital image-based numerical modeling method for prediction of inhomogeneous rock failure", *Int. J. Rock Mech. Min. Sci.*, **41**(6), 939-957. https://doi.org/10.1016/j.ijrmms.2004.03.002.

Chiou, Y.J., Lee, Y.M. and Tsay, R.J. (2002), "Mixed mode fracture propagation by manifold method", *Int. J. Fract.*, **114**(4), 327-347. https://doi.org/10.1023/A:1015713428989.

Cook, N.G. (1965), "The failure of rock", *Int. J. Rock Mech. Min. Sci. Geomech.*, Pergamon, December.

Goodman, R.E., Taylor, R.L. and Brekke, T.L. (1968), "A model for the mechanics of jointed rock", *J. Soil Mech. Found. Division*, **94**(3), 637-659. https://doi.org/10.1061/JSFEAQ.0001133.

Huang, D., Liu, Y., Yang, Y., Li, Z. and Meng, Q. (2021), "Experimental study on three-point-bending characteristics of hard and soft rock-like materials under different loading rates", *Arabian J. Geosci.*, **14**, 1-12. https://doi.org/10.1007/s12517-021-08284-9.

Jiao, Y., Huang, G., Zhao, Z., Zheng, F. and Wang, L. (2015), "An improved three-dimensional spherical DDA model for simulating rock failure", *Science China Technol. Sci.*, **58**(9), 1533-1541. https://doi.org/10.1007/s11431-015-5898-9.

Katona, M.G. (1983), "A simple contact–friction interface element with applications to buried culverts", *Int. J. Numer. Anal. Method. Geomech.*, **7**(3), 371-384. https://doi.org/10.1002/nag.1610070308.

Li, J., Khodaei, Z.S. and Aliabadi, M.H. (2017), "Spectral bem for the analysis of wave propagation and fracture mechanics", *J. Multiscale Modell.*, **8**(3-4), 1740007. https://doi.org/10.1142/S1756973717400078.

Lim, I.L., Johnston, I.W. and Choi, S.K. (1993), "Stress intensity factors for semi-circular specimens under three-point bending", *Eng. Fract. Mech.*, **44**(3), 363-382. https://doi.org/10.1016/0013-7944(93)90030-V.

Liao, Z.Y., Zhu, J.B. and Tang, C.A. (2019), "Numerical investigation of rock tensile strength determined by direct tension, Brazilian and three-point bending tests", *Int. J. Rock Mech. Min. Sci.*, **115**, 21-32. https://doi.org/10.1016/j.ijrmms.2019.01.007.

Liu, X., Hu, C., Liu, Q. and He, J. (2021), "Grout penetration process simulation and grouting parameters analysis in fractured rock mass using numerical manifold method", *Eng. Anal. Bound. Elem.*, **123**, 93-106. https://doi.org/10.1016/j.enganabound.2020.11.008.

Ma, G.W. and An, X.M. (2008), "Numerical simulation of blasting-induced rock fractures", *Int. J. Rock Mech. Min. Sci.*, **45**(6), 966-975. https://doi.org/10.1016/j.ijrmms.2007.12.002.

Ma, G.W., An, X.M., Zhang, H.H. and Li, L. (2009), "Modeling complex crack problems using the numerical manifold method", *Int. J. Fracture*, **156**(1), 21-35. https://doi.org/10.1007/s10704-009-9342-7.

Ma, G., An, X. and He, L.E.I. (2010), "The numerical manifold method: a review", *Int. J. Comput. Method.*, **7**(1), 1-32. https://doi.org/10.1142/S0219876210002040.

Ma, G.W., Wang, X.J. and Ren, F. (2011), "Numerical simulation of compressive failure of heterogeneous rock-like materials using SPH method", *Int. J. Rock Mech. Min. Sci.*, **48**(3), 353-363. https://doi.org/10.1016/j.ijrmms.2011.02.001.

Melin, S. (1989), "Why are crack paths in concrete and mortar different from those in PMMA?", *Mater. Struct.*, **22**(127), 23-27. https://doi.org/10.1007/BF02472691.

Ouchi, H., Katiyar, A., Foster, J.T. and Sharma, M.M. (2015), "A peridynamics model for the propagation of hydraulic fractures in heterogeneous, naturally fractured reservoirs", *Proceedings of the SPE Hydraulic Fracturing Technology Conference and Exhibition*, SPE, February.

Patil, R.U., Mishra, B.K. and Singh, I.V. (2019), "A multiscale framework based on phase field method and XFEM to simulate fracture in highly heterogeneous materials", *Theor. Appl. Fract. Mech.*, **100**, 390-415. https://doi.org/10.1016/j.tafmec.2019.02.002.

Shi, G.H. (1991), "Manifold method of material analysis", *Proceedings of the Transactions of the 9th army conference on applied mathematics and computing*, Minneapolis, June.

Schlangen, E. and Van Mier, J. (1992), "Experimental and numerical analysis of micromechanisms of fracture of cement-based composites", *Cement Concrete Compos.*, **14**(2), 105-118. https://doi.org/10.1016/0958-9465(92)90004-F.

Shemirani, A.B., Haeri, H., Sarfarazi, V. and Hedayat, A. (2017), "A review paper about experimental investigations on failure behaviour of non-persistent joint", *Geomech. Eng.*, **13**(4), 535-570. https://doi.org/10.12989/gae.2017.13.4.535.

Shi, J.W., Fu, Z.Z. and Guo, W.L. (2019), "Investigation of geometric effects on three-dimensional tunnel deformation mechanisms due to basement excavation", *Comput. Geotech.*, **106**, 108-116. https://doi-org/ 10.1016/j.compgeo.2018.10.019.

Shi, J.W., Chen Y.H., Lu, H., Ma, S.K. and Ng, C.W.W. (2022), "Centrifuge modeling of the influence of joint stiffness on pipeline response to underneath tunnel excavation", *Can. Geotech. J.*, **59**(9), 1568-1586. https://doi.org/10.1139/cgj-2020-0360.

Shi, J.W., Wang, J.P., Chen Y.H., Shi, C., Lu, H., Ma, S.K. and Fan, Y.B. (2023), "Physical modeling of the influence of tunnel active face instability on existing pipelines", *Tunn. Undergr. Sp. Tech.*, **140**, 105281. https://doi.org/10.1016/j.tust.2023.105281.

Strouboulis, T., Copps, K. and Babuška, I. (2000), "The generalized finite element method: an example of its implementation and illustration of its performance", *Int. J. Numer. Meth. Eng.*, **47**(8), 1401-1417. https://doi.org/10.1002/(SICI)10970207(20000320)47:8<1401::AID-NME835>3.0.CO;2-8.

Strouboulis, T., Copps, K. and Babuška, I. (2001), "The generalized finite element method", *Computer Method. Appl. M.*, **190**(32-33), 4081-4193. https://doi.org/10.1016/S0045-7825(01)00188-8.

Tang, C. (1997), "Numerical simulation of progressive rock failure and associated seismicity", *Int. J. Rock Mech. Min. Sci.*, **34**(2), 249-261. https://doi.org/10.1016/S0148-9062(96)00039-3.

Tang, C.A., Yang, W.T., Fu, Y.F. and Xu, X.H. (1998), "A new approach to numerical method of modelling geological processes and rock engineering problems—continuum to discontinuum and linearity to nonlinearity", *Eng. Geol.*, **49**(3-4), 207-214. https://doi.org/10.1016/S0013-7952(97)00051-3.

Tang, C.A., Liu, H., Lee, P.K.K., Tsui, Y. and Tham, L. (2000), "Numerical studies of the influence of microstructure on rock failure in uniaxial compression—part I: effect of heterogeneity", *Int. J. Rock Mech. Min. Sci.*, **37**(4), 555-569. https://doi.org/10.1016/S1365-1609(99)00121-5.

Tang, C.A., Tham, L.G., Lee, P.K.K., Tsui, Y. and Liu, H. (2000), "Numerical studies of the influence of microstructure on rock failure in uniaxial compression—part II: constraint, slenderness and size effect", *Int. J. Rock Mech. Min. Sci.*, **37**(4), 571-583. https://doi.org/10.1016/S1365-1609(99)00122-7.

Tang, X. and Zhang, C. (2009), "Meso-scale modeling of concrete: Effects of heterogeneity", *J. Hydroelectric Eng.*, **28**(4), 56-62.

Tang, S. (2011), "Applications of rock failure process analysis (RFPA) method", *J. Rock Mech. Geotech. Eng.*, **3**(4), 352-372. https://doi.org/10.3724/SP.J.1235.2011.00352.

Tsang, Y.W. and Witherspoon, P.A. (1981), "Hydromechanical behavior of a deformable rock fracture subject to normal stress", *J. Geophys. Res. Solid Earth*, **86**(10), 9287-9298. https://doi.org/10.1029/JB086iB10p09287.

Wang, S.L., Feng, X.T. and Ge, X.R. (2003), "Study on crack propagation modeling by high order manifold method", *Rock Soil Mech.-Wuhan-*, **24**(4), 622-625. https://doi.org/10.16285/j.rsm.2003.04.033.

Wang, X., Yuan, W., Yan, Y.T. and Zhang, X. (2020), "Scale effect of mechanical properties of jointed rock mass: a numerical study based on particle flow code", *Geomech. Eng.*, **21**(3), 259-268. https://doi.org/10.12989/gae.2020.21.3.259.

Wu, Z., Fan, L., Liu, Q. and Ma, G. (2017), "Micro-mechanical modeling of the macro-mechanical response and fracture behavior of rock using the numerical manifold method", *Eng. Geol.*, **225**, 49-60. https://doi.org/10.1016/j.enggeo.2016.08.018.

Wu, Z., Yu, F., Zhang, P. and Liu, X. (2019), "Micro-mechanism study on rock breaking behavior under water jet impact using coupled SPH-FEM/DEM method with Voronoi grains", *Eng. Anal. Bound. Elem.*, **108**, 472-483. https://doi.org/10.1016/j.enganabound.2019.08.026.

Wu, W., Zheng, H. and Yang, Y. (2019), "Enriched three-field numerical manifold formulation for dynamics of fractured saturated porous media", *Comput. Method. Appl. M.*, **353**, 217-252. https://doi.org/10.1016/j.cma.2019.05.008.

Wu, W., Yang, Y. and Zheng, H. (2020), "Enriched mixed numerical manifold formulation with continuous nodal gradients for dynamics of fractured poroelasticity", *Appl. Math. Modell.*, **86**, 225-258. https://doi.org/10.1016/j.apm.2020.03.044.

Wu, W., Yang, Y. and Zheng, H. (2020), "Hydro-mechanical simulation of the saturated and semi-saturated porous soil—rock mixtures using the numerical manifold method", *Comput. Method. Appl. Mech. Eng.*, **370**, 113238. https://doi.org/10.1016/j.cma.2020.113238.

Xiong, X., Li, B., Jiang, Y., Koyama, T. and Zhang, C. (2011), "Experimental and numerical study of the geometrical and hydraulic characteristics of a single rock fracture during shear", *Int. J. Rock Mech. Min. Sci.*, **48**(8), 1292-1302. https://doi.org/10.1016/j.ijrmms.2011.09.009.

Xue, Y.C., Sun, W.B. and Wu, Q.S. (2020), "The influence of magmatic rock thickness on fracture and instability law of mining surrounding rock", *Geomech. Eng.*, **20**(6), 547-556. https://doi.org/10.12989/gae.2020.20.6.547.

Yang, Y., Tang, X., Zheng, H., Liu, Q. and He, L. (2016), "Three-dimensional fracture propagation with numerical manifold method", *Eng. Anal. Bound. Elem.*, **72**, 65-77. http://dx.doi.org/10.1016/j.enganabound.2016.08.008.

Yang, Y., Tang, X., Zheng, H., Liu, Q. and Liu, Z. (2018), "Hydraulic fracturing modeling using the enriched numerical manifold method", *Appl. Math. Modell.*, **53**, 462-486. https://doi.org/10.1016/j.apm.2017.09.024.

Yang, Y., Xu, D., Liu, F. and Zheng, H. (2020), "Modeling the entire progressive failure process of rock slopes using a strength-based criterion", *Comput. Geotech.*, **126**, 103726. https://doi.org/10.1016/j.compgeo.2020.103726.

Yang, B., Cao, X., Han, T., Li, P. and Shi, J. (2022), "Effect of heterogeneity on the extension of ubiquitiformal cracks in rock materials", *Fractal Fractional*, **6**(6), 317. https://doi.org/10.3390/FRACTALFRACT6060317.

Yu, C.Y., Zheng, F., Guo, B.C. and Liu, Q.Y. (2020), "A generalized cover renewal strategy for multiple crack propagation in two-dimensional numerical manifold method", *J. Central South Univ.*, **27**(8), 2367-2381. https://doi.org/10.1007/s11771-020-4455-2.

Zhang, G.X., Sugiura, Y., Hasegawa, H. and Wang, G. (2002), "The second order manifold method with six node triangle mesh", *Struct. Eng. Earthq. Eng.*, **19**(1), 1-9. https://doi.org/10.2208/jsceseee.19.1s.

Zhang, H.H., Li, L.X., An, X.M. and Ma, G. (2010), "Numerical analysis of 2-D crack propagation problems using the numerical manifold method", *Eng. Anal. Bound. Elem.*, **34**(1), 41-50. https://doi.org/10.1016/j.enganabound.2009.07.006.

Zhou, X.P., Cheng, H. and Feng, Y.F. (2014), "An experimental study of crack coalescence behaviour in rock-like materials containing multiple flaws under uniaxial compression", *Rock Mech. Rock Eng.*, **47**(6), 1961-1986. https://doi.org/10.1007/s00603-013-0511-7.

Zhu, W.C. and Tang, C.A. (2004), "Micromechanical model for simulating the fracture process of rock", *Rock Mech. Rock Eng.*, **37**, 25-56. https://doi.org/10.1007/s00603-003-0014-z.

Zhu, W.C. and Tang, C.A. (2006), "Numerical simulation of Brazilian disk rock failure under static and dynamic loading", *Int. J. Rock Mech. Min. Sci.*, **43**(2), 236-252. https://doi.org/10.1016/j.ijrmms.2005.06.008.

Zi, G. and Belytschko, T. (2003), "New crack-tip elements for XFEM and applications to cohesive cracks", *Int. J. Numer. Meth. Eng.*, **57**(15), 2221-2240. https://doi.org/10.1002/nme.849.

GC